RESEARCH PAPER

Numerical simulation of arc and metal transfer behaviors in double-wire gas metal arc welding

Jie Xu[1] · Yiming Ma[1] · Lin Wang[1] 🅞 · Xu Lu[2]

Abstract

The three-dimensional coupled arc-droplet models for traditional single-wire gas metal arc welding (SW-GMAW) and double-wire gas metal arc welding (DW-GMAW) were established. The mutual attraction of two arcs and the inclination of the droplets in DW-GMAW were analyzed numerically. The temperature, fluid flow velocity, and electromagnetic force distributions were compared between DW-GMAW and SW-GMAW. Compared with SW-GMAW, the temperature distribution on the workpiece surface was bimodal along x-axis and the peak temperature reduced in DW-GMAW. The high-temperature region in the filler metal was decreased dramatically. The fluid flow mode of the arc plasma in DW-GMAW was changed, and the peak velocity of the arc plasma decreased. Besides, the forces acted on the arc plasma were compared and the reason for the arc inclination was analyzed. Experimental data was used to validate the model's predictions.

Keywords Coupled model · Numerical simulation · Gas metal arc welding · Double wire · Arc plasma · Metal transfer · Electromagnetic force distributions

1 Introduction

Wire arc additive manufacturing (WAAM) has projecting ascendancy on producing large structure parts because of its characteristics such as high deposition rate, low energy consumption, competitive cost of machine, and reduced material wastage compared to other additive manufacturing technologies [1–4]. Gas metal arc welding (GMAW)-based additive manufacturing is one of the common WAAM methods. In order to increase the welding efficiency of GMAW, many high-efficiency welding method or process variants have been developed with the GMAW as the basis such as TIG-MIG hybrid welding [5, 6], laser-MIG hybrid welding [7], double- or multi-wire/electrode welding [8–11], and external magnetic field–assisted welding [12, 13]. Due to the high melting efficiency, high adaptability, and low cost of two-wire welding technique, it had a widespread adoption in welding manufacturing [14, 15] and wire arc additive

manufacturing (WAAM) [16, 17]. Double-wire gas metal arc welding (DW-GMAW) is a common two-wire welding, and two arcs are formed between the wires and the molten pool during this process. On one hand, the melting and deposition of two wires increased the efficiency of welding or additive manufacturing. On the other hand, two arcs between the wires and molten pool can change the heat input distribution to improve the appearance or the quality of the deposited parts. However, because the distance between two wires is very short, the two arcs are easily interfered by the other one with the influence of the electromagnetic force. As a consequence, the droplet transfer and weld pool behaviors will be affected by the arc characteristics. Thus, two arc interactions and metal transfer play a critical role in the process stability as well as welding/WAAM quality [18–20].

Recently, many researchers have paid attention to the investigation on arc characteristics and metal transfer behaviors to get better understanding of DW-GMAW. Ueyama et al. [21] experimentally studied the effect of CO_2 mixture ratio and inter-wire distance on the arc interruption and arc voltage in tandem pulsed GMAW. Moinuddin et al. [22] found that different currents at two wires could induce the arc stability in anti-phase synchronized synergic-pulsed DW-GMAW. Chen et al. [18] studied the influence of phase difference of the welding current between two wires on the arc interruption and weld pool, and they suggested

✉ Lin Wang
wanglin1990@cumt.edu.cn

1   School of Materials Science and Physics, China University of Mining and Technology, Xuzhou 221116, China

2   FAW Jiefang Automotive Company, Ltd. Qingdao Auto Factory, Qingdao 266043, China

that the frequency of arc interruption could increase with the increase of phase difference. Groetelaars et al. [23] studied the influence of arc length on droplet transfer and the results showed that the increase of arc length can modify the metal transfer mode from short circuit to spay. Cai et al. [24] found that the arc was expanded and the arc length increased when the content of CO_2 or helium increased in narrow gap tandem GMAW. Wu et al. [25] found that the joint effects of the electromagnetic field, arc pressure, and arc stiffness caused the arc offset, and smaller phase difference resulted in shallower penetration and larger weld width in high-power double-wire double pulsed GMAW.

Understanding the interaction mechanism of two arcs and its influence on metal transfer is helpful to further control and improve DW-GMAW process. Numerical simulation is an economical, time-saving, and intuitive method to analyze the internal mechanism of welding process. Some researchers also proposed some numerical models of DW-GMAW. For example, Pu et al. [26] numerically analyzed the influence of welding current on temperature, velocity, and pressure fields on workpiece surface in tandem GMAW. Schnick et al. [27] established a numerical model to simulate the interaction of two arcs and their influence on the flow status of shielding gas in pulsed tandem GMAW. The emphasis of their study was on the interactions between the two arcs under the anti-phase-synchronized pulsed current so the model did not consider the formation of droplet. Ding et al. established two three-dimensional mathematical models for the droplet [28] and arc [29], respectively. The arc and metal transfer behaviors between single-wire gas metal arc welding (SW-GMAW) and DW-GMAW were compared, respectively. However, the interaction of heat and force between arc plasma and filler metal was simplified drastically. A unified model containing arc plasma and metal transfer is necessary to deeply investigate the interaction between two arcs and between the arc and filler metal for DW-GMAW.

In this study, a three-dimensional model was established by considering the interaction of two arcs and filler metal in SW-GMAW and DW-GMAW with constant welding current. The arc plasma characteristics and metal transfer process in DW-GMAW was simulated and compared with traditional SW-GMAW. The arc temperature, arc plasma flow, and droplet temperature were predicted and compared in SW-GMAW and DW-GMAW. This study laid the foundation for the further understanding of DW-GMAW/WAAW and their process optimization.

2 Mathematic model

2.1 Basic assumptions

The aim of this study is to investigate the interaction of the two arcs and its influence on metal transfer, so the following

assumptions were conducted for the simplification of the model. The arc plasma was in local thermodynamic equilibrium (LTE) and optically thin, and the arc plasma and the metal were incompressible and the fluid flow was laminar [30–33]. The wire axis was assumed to be vertical, and its slope angle was not considered [28, 29]. The mass loss of the molten metal was ignored, and the metal vapor was not considered [27, 34, 35]. Many experimental and theoretical investigations demonstrated that the iron vapor had a dominant influence in GMAW arcs with steel electrodes, with a local temperature minimum occurring on the arc axis due to the strong radiation from iron atoms and ions [30, 36, 37]. And the reduced temperature near the arc axis reduced the electrical conductivity, which further influenced the arc-wire attachment. Detailed numerical investigations on arc-wire attachment in GMAW under the influence of metal vapor have been reported by Ogino et al. [38, 39]. However, in this study, we mainly discussed the difference on the arc and droplet behaviors between SW-GMAW and DW-GMAW by numerical simulation. Although the accuracy of simulated arc temperature was affected as a consequence of the ignorance of metal vapor, the comparison of temperature difference between single-wire GMAW and double-wire GMAW had the theoretical meaning in understanding the arc interactions and its influence on metal transfer in DW-GMAW.

2.2 Governing equations and source terms

(a) Mass continuity equation:

$$\frac{\partial \rho}{\partial t} + \nabla \bullet \left(\rho \vec{V} \right) = 0 \tag{1}$$

(b) Momentum conservation:

$$\frac{\partial (p\vec{v})}{\partial t} + \nabla (p\vec{v}\vec{v}) = -\nabla p + \nabla \bullet \left(\overline{\overline{\tau}} \right) + p\vec{g} + \vec{j} \times \vec{B} + \vec{F}_{ST} \tag{2}$$

(c) Energy conservation:

$$\frac{\partial (pH)}{\partial t} + \nabla \bullet \left(p\vec{v}H \right) = \nabla \bullet (\lambda \nabla T) + \frac{\left| \vec{j} \right|^2}{\sigma} + S \tag{3}$$

(d) Electric potential:

$$\nabla \bullet (\sigma \nabla \phi) = 0 \tag{4}$$

(e) Magnetic vector potential:

$$\nabla^2 \vec{A} = -\mu_0 \vec{j} \tag{5}$$

(f) Ohm's law:

$$\vec{j} = -\sigma \bullet \nabla \phi \tag{6}$$

(g) Magnetic field:

$$\vec{B} = \nabla \times \vec{A} \tag{7}$$

In Eqs. (1)–(10), ρ, t, p, $\overline{\overline{\tau}}$, H, λ, T, σ, μ_0, and ϕ are, density, time, pressure, stress tensor, enthalpy, thermal conductivity, temperature, electrical conductivity, magnetic permeability, and electric potential respectively. $\vec{V}$, $\vec{g}$, $\vec{j}$, $\vec{B}$, and $\vec{A}$ are the velocity vector, the acceleration due to gravity, welding current density, magnetic flux density, and magnetic vector potential, respectively. $\vec{F}_{ST}$ represents the surface tension force, which was calculated using the continuum surface force (CSF) [40] method by transferring it into the volume force in the surface of liquid metal.

In Eq. (3), the second term on the right-hand side is Ohmic heating and the last term is the additional energy source. In the arc region, the heat transfer associated with the electron transfer enthalpy and the radiation loss was considered, so the third term S of Eq. (3) was obtained from the following equation:

$$S = \frac{5K_B}{2e} \left| \vec{j} \right| \cdot \nabla T - S_R \tag{8}$$

where K_B, e, and S_R are the Boltzmann constant, electron charge, and the radiation loss, respectively. The accurate calculation of radiation loss within the arc is extremely difficult. For welding arcs, the radiation loss energy is generally less than 20% of the total input energy. In addition, since the temperature of most arc plasmas is less than 20 000 K, the proportion of radiation in the vacuum ultraviolet is very small. Therefore, a simple net emission coefficient was used to calculate the radiation loss without considering the self-absorption effect of arc center radiation in the out-of-arc region [41, 42]. In this study, S_R was calculated by the following equation:

$$S_R = -4\pi\varepsilon_n \tag{9}$$

where ε_n is net emission coefficient.

There exists a sheath layer at the plasma-electrode interface, which deviates from the thermo-dynamic equilibrium state. According to the research by Murphy et al. [30, 31, 43], an additional energy sources term was added to consider its heating effects, which was called "LTE-diffusion approximation" method. The energy sources term was added as follows [44]:

$$S = j_a V_a + j_a \varphi_a - \varepsilon \alpha T^4 \tag{10}$$

where j_a and V_a are the voltage fall in the anode sheath and φ_a, ε, and α are the work function, the emissivity of the wire surface, and the Stefan-Boltzmann constant, respectively.

The interface of gas and metal phases was tracked by the volume-of-fluid method [40, 45] in the simulation:

$$\frac{dF_m}{dt} = \frac{\partial F_m}{\partial t} + \left(\vec{v} \cdot \nabla F_m \right) = 0 \tag{11}$$

The cell volume of fluid fraction F_m was introduced to calculate the gas–liquid interface. For two-phase flow of metal and gas, the cell is full of metal if F_m is equal to 1. The cell is full of gas if F_m is equal to 0. The cell presents the metal-gas interface if F_m is between 0 and 1. In this model, the geometric reconstruction scheme was used to determine the interface profile. It assumes that the interface between two fluids has a linear slope within each cell, which is used to calculate the advection of fluid through the cell faces.

2.3 Calculation domain and boundary conditions

To compare the arc and droplet transfer behaviors between SW-GMAW and DW-GMAW, two numerical models with the same dimension were constructed. Figures 1 and 2 show the calculation domains for SW-GMAW and DW-GMAW, respectively. The dimensions of two domains were 30.0 mm $(x) \times 20.0$ mm $(y) \times 22.0$ mm (z). The diameter of the wires was 1.2 mm. The distance from the wire tip to the workpiece surface was 10.0 mm. For DW-GMAW, the distance between two wire axes was 10.0 mm. The boundary conditions for the domains are listed in Table 1. The shielding gas flowed into the calculated domain from the upper surface (gas inflow) with a vertical velocity component (v_z) was considered [46, 47]. The wire tip was the inlet of the molten filler metal by ignoring the melting process of the solid wire, and its inflow velocity was regarded as wire melting rate (v_{wire}), which was estimated by the empirical equation [48]. Due to the ignorance of the melting process of filler wire, the consumed energy of the wire from solid to molten state was considered and deducted by calculate the valid value of current density (j_z) that applied on the wire tip. The valid current density applied on wire tips was calculated by the following equation:

$$\vec{j}_z = \frac{U \times I - C_{pw} \times \rho_w \times \pi R_w^2 \times v_{wire} \times \Delta T - \Delta H_w \times \rho_w \times \pi R_w^2 \times v_{wire}}{\pi R_w^2 \times U} \tag{12}$$

where U represents the arc voltage, I represents the welding current, and ΔT is the difference between the melting point of the wire and the room temperature. C_{pw}, ρ_w, and ΔH_w are the specific heat, density, and fusion latent heat of the filler wire, respectively.
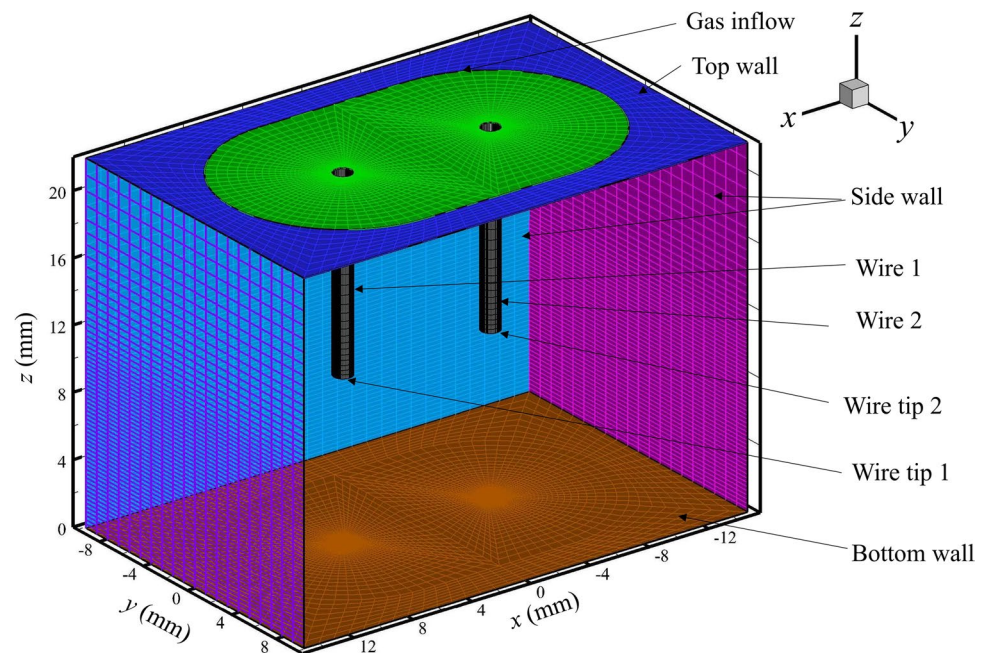
2.4 Numerical considerations

In this study, a two-phase model (arc plasma and filler metal) was used. If the transient solution was chosen directly to calculate the arc and droplet, the arc was not steady and its maximum exceeded 50,000 K in the initial stage. Under this

Fig. 1 Calculation domain in SW-GMAW
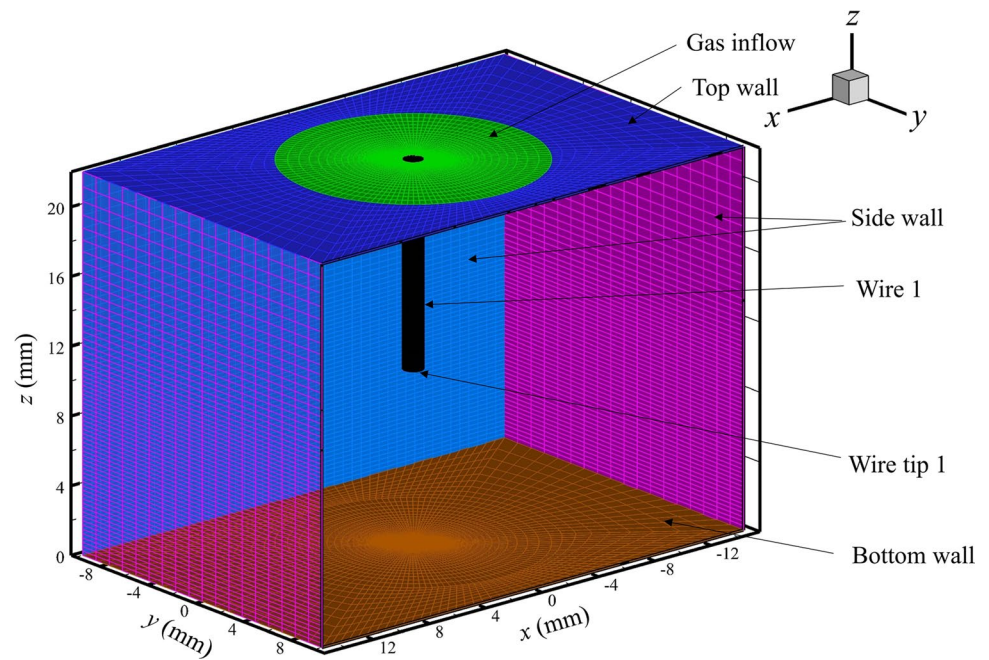
Fig. 2 Calculation domain in DW-GMAW

condition, the calculated droplet size and temperature were not accurate. Therefore, the steady solution was activated at first to only simulate the arc plasma without the consideration of filler metal. Both the wire tip 1 and wire tip 2 were set as wall boundary, which meant that no metal phase flowed into the computational domain. When the solution was converged, the steady arcs were obtained. After that, the transient model was activated. The wire tip 1 and wire tip 2 were changed to be velocity inlet of metal phase. So the filler metal could flow into the domain from the wire tips to

form the droplet. In this study, the simulation was calculated by the CFD software ANSYS Fluent 15.0. A pressure-based solver and a transient calculation method were used. The used time step size was 5×10^{-6} s.

Pure argon (Ar) was used as the shielding gas, and its physical properties were assumed to be only temperature-dependent; the detailed data were from the references [49, 50]. The physical properties of the welding wire were considered the same with that of the base metal (mild steel,

Table 1 Boundary conditions

Boundary	T	v	φ	A
Gas inflow	300 K	v_z	$\frac{\partial \phi}{\partial n} = 0$	$\frac{\partial \vec{A}}{\partial n} = 0$
Wire tip 1	1800 K	$v_z = v_{wire}$	$\sigma \frac{\partial \phi}{\partial n} = j_z$	$\frac{\partial \vec{A}}{\partial n} = 0$
Wire tip 2	1800 K	$v_z = v_{wire}$	$\sigma \frac{\partial \phi}{\partial n} = j_z$	$\frac{\partial \vec{A}}{\partial n} = 0$
Top wall	300 K	—	$\frac{\partial \phi}{\partial n} = 0$	0
Outflow	300 K	—	$\frac{\partial \phi}{\partial n} = 0$	0
Bottom wall	1000 K	—	$\phi = 0$	$\frac{\partial \vec{A}}{\partial n} = 0$

Q235) [47]. The used welding current was 210A, and the flow rate of the shielding gas (pure argon) was 15 L/min.

3 Results and discussion

The arc plasma and metal transfer behaviors during the SW-GMAW process were simulated at first. Figure 3 shows the calculated arc temperature isotherms and the metal transfer at the *xoz* section across the wire axis. The trajectory of the droplet transfer was vertical along the vertical direction. The arc temperature was symmetric along wire axis, and the arc was restricted to be bell-shaped due to the electromagnetic pinch force. The high-temperature region was around the undetached filler metal, and the maximum temperature was 18,290 K.

During the DW-GMAW process, the arc temperature and metal transfer at the *xoz* section across are displayed in

Fig. 4. Two arcs were attracted to each other, and the filler metal was also inclined to each other due to the arc attraction. The maximum temperature of the arcs was decreased to 16,930 K. Figure 5 displays the comparison of temperature on the workpiece surface for SW-GMAW and DW-GMAW at $t = 0$ s. Along *y*-axis, the temperature distribution for SW-GMAW was unimodal and the peak temperate was 12,110 K, which was directly beneath the wire ($y = 0$). For DW-GMAW, the temperature was also unimodal distribution along *y*-axis, but the peak temperate was decreased to 6792 K. Along *x*-axis, the temperature distribution for SW-GMAW was still unimodal with a peak temperate of 12,110 K. For DW-GMAW, the temperature distribution became bimodal and the peak temperature was reduced to 7763 K. Besides, the peak temperature points were deviated from the wire axis ($y = \pm 5.0$ mm) and located on the points of $y = \pm 2.2$ mm due to the attraction of two arcs.

The arc temperature is closely associated with the fluid flow of arc plasma. Figure 6 shows the fluid flow velocity of the arc plasma for SW-GMAW. The velocity distribution was axisymmetric along the wire centerline. The arc plasma flowed downwards to the workpiece surface and then veered and flowed outwards after it impacted the workpiece surface with very high velocity. Meanwhile, the energy of the plasma was transported to the workpiece from the upper part with the arc plasma flow. Because the arc plasma flowed radially top-down in SW-GMAW, so the temperature on the workpiece was of Gaussian distribution; that is, the temperature was highest in the center and gradually decreased in all directions. However, in DW-GMAW, the velocity field of arc plasma was markedly different from that in SW-GMAW due to the interattraction of two arcs. As displayed in Fig. 7, the
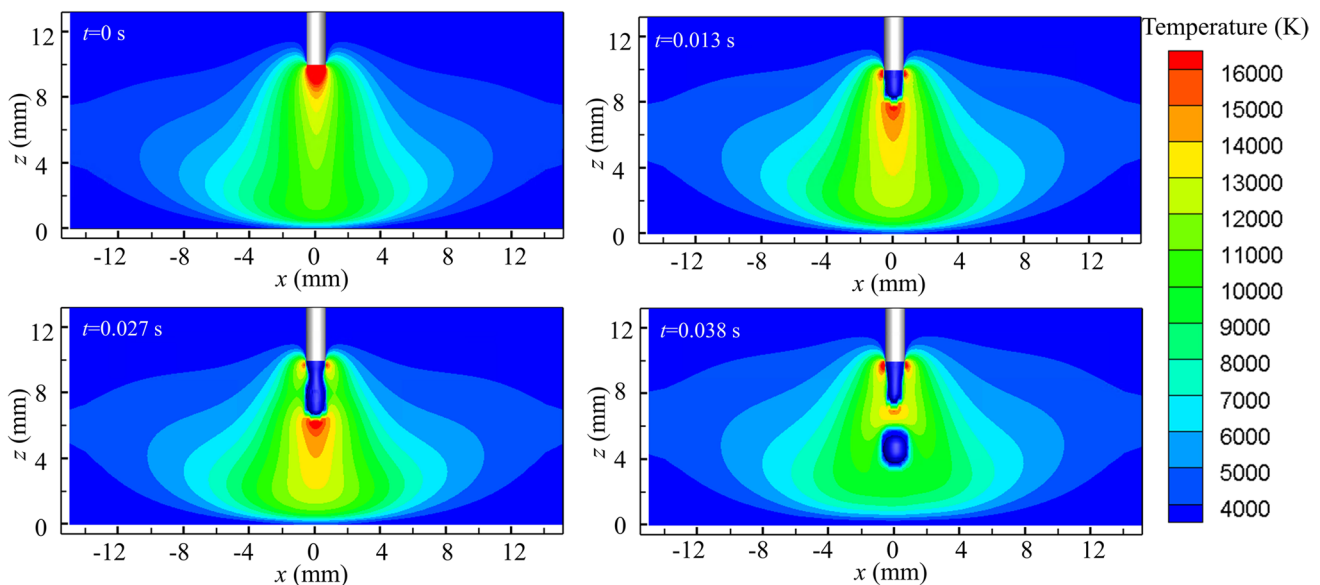
**Fig. 3** Simulated arc temperature in SW-GMAW
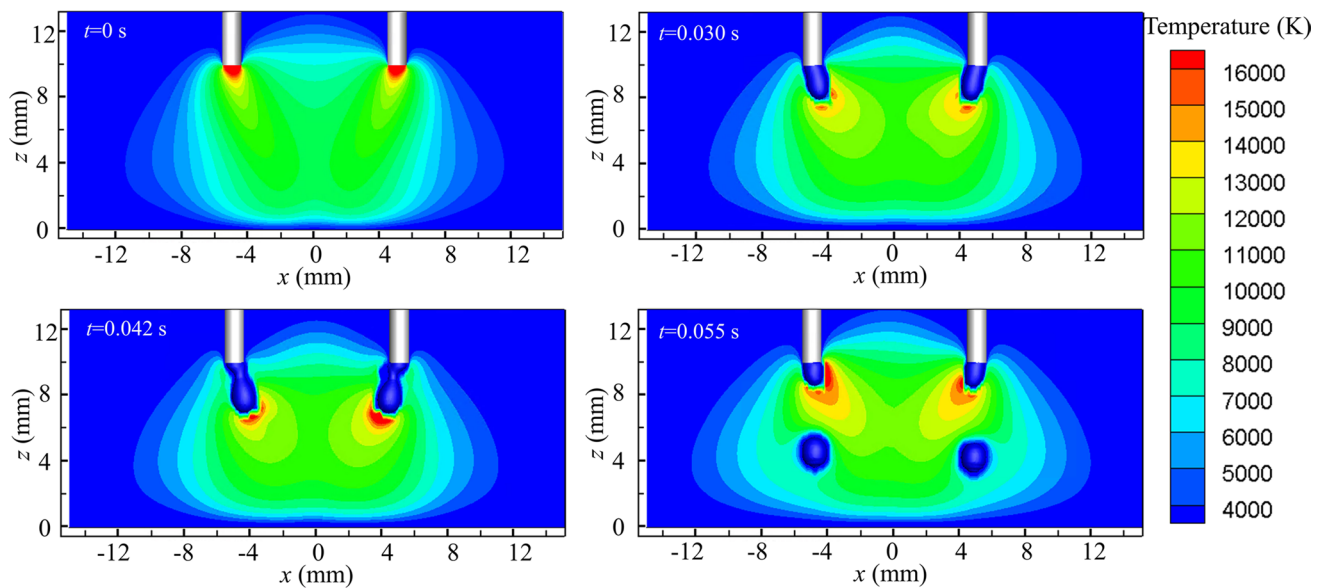
Fig. 4 Simulated arc temperature in DW-GMAW

arc plasma from two electrodes flowed inward to the center of the domain and two arc plasma flows were converged at the center of two wires and then changed their direction. One part flowed downward to the workpiece surface and the other flowed upward, which caused part of the energy was taken away with the upward arc plasma flow. As a consequence, the maximum temperature on the workpiece was lower in DW-GMAW than SW-GMAW. Besides, the temperature distribution became bimodal because the inclination angles of two arc was smaller. With the decrease of the distance of two wires or the increase of the welding currents, the interactions of two arc will become more intense, and the temperature distribution will become unimodal. The relation between the welding parameters and temperature distribution will be investigated in our future research.

In SW-GMAW, the velocity of arc plasma reached its peak level under the wire tip and the peak velocity was 98 m/s. However, the peak velocity of the arc plasma in DW-GMAW was decreased to 71 m/s compared with SW-GMAW. The arc shape and arc plasma velocity were associated with the force state. Consequently, the electromagnetic force distributions of the arc plasma were compared between SW and DW-GMAW. Figure 8 shows the self-induced electromagnetic force distribution for SW-GMAW. The self-induced electromagnetic force was distributed symmetrically along the wire centerline. The direction of the self-induced electromagnetic force was top-down from the outside to the arc center. Moreover, its magnitude near the filler metal tip was much larger than the bottom of the arc so the arc can be constricted to be bell-shaped. Figure 9 displays the electromagnetic force distribution for DW-GMAW. For each arc, the electromagnetic force was still pointing to the arc center

to constrict the arc. However, the component of the inward electromagnetic force was increased and its direction is from the arc to other one, which caused the mutual attraction of two arcs. Under this condition, the downward component of electromagnetic force decreased due to the attraction of two arcs. The downward acceleration of the arc plasma was reduced so the vertical velocity decreased compared with SW-GMAW. Therefore, the maximum plasma velocity in DW-GMAW is less than that in SW-GMAW.

Figure 10 displays the schematic diagram of generated electromagnetic force in two arcs. Taking the left-side arc (arc 1) as an example, the electromagnetic force acted on this arc can be divided into two parts. The first part is called self-induced electromagnetic force (F_{s1}), which was generated by the interaction of the current density and self-induced magnetic field excited by the current (I_1) between the wire 1 and workpiece. The other part is called additional electromagnetic force (F_{e1}), which was produced from the interaction of the current density and induced magnetic field by the current (I_2) between the wire 2 and workpiece. Figure 11 shows the magnitudes of the two forces along x direction at 4 mm above the workpiece surface. The magnitude of F_{e1} was slightly lower than F_{s1}, but they have the same order of magnitude. The value of F_{s1} was positive at $x < -2.0$ mm and was negative at $x > -2.0$ mm. So the direction of F_{s1} was pointing to the positive x-axis at $x < -2.0$ mm and the negative x-axis at $x > -2.0$ mm, which means that F_{s1} can make the arc 1 keep constricted, as shown in Fig. 10. However, the value of F_{e1} was always positive in the whole arc 1 region ($x < 2.0$ mm), so its direction was pointing to the positive x-axis, which can lead to the tilt of the arc. The tilt angle of the arcs was closely related to the two electromagnetic
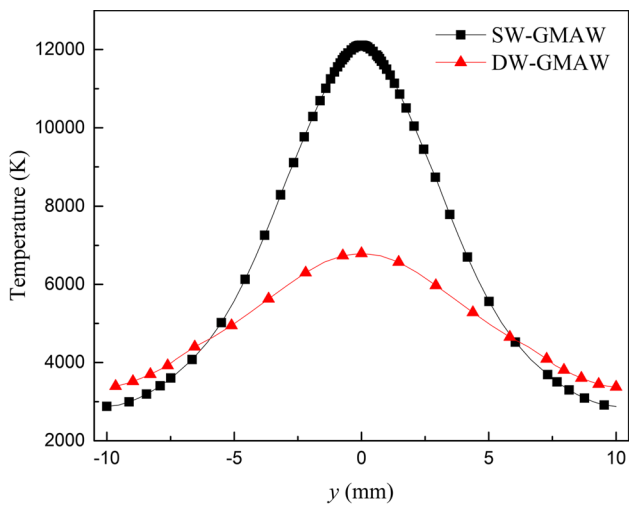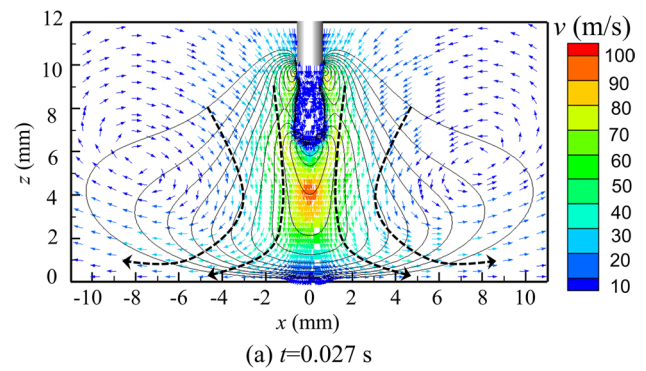
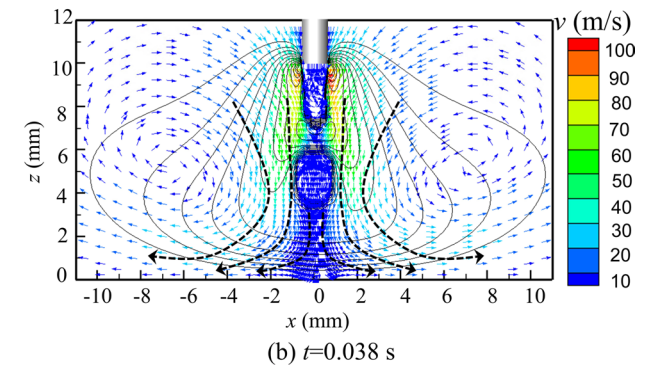(a) Along y-axis (x=0 mm)
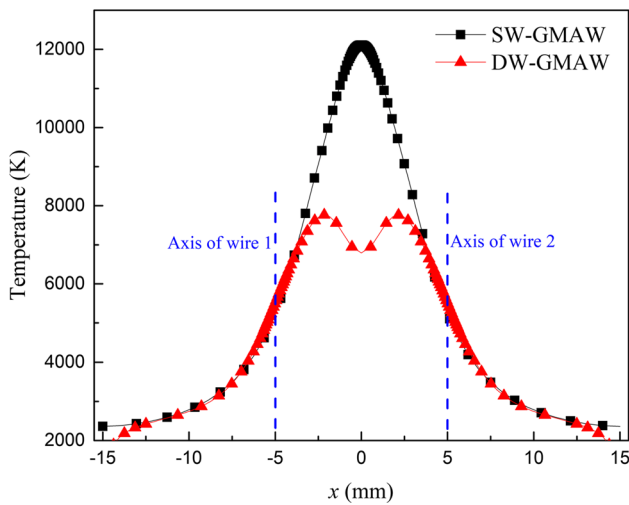
(b) Along x-axis (y=0 mm)

Fig. 5 Comparison of temperature on the workpiece surface

(a) t=0.027 s

(b) t=0.038 s

Fig. 6 Velocity distribution in SW-GMAW

(a) t=0.042 s

(b) t=0.055 s

Fig. 7 Velocity distribution in DW-GMAW

forces, and the two forces were associated with the welding current, distance between two wires, shielding gas, etc., which needs to be further investigated in the future work.

The arc attraction also has influence on the temperature of the filler metal in DW-GMAW. Figure 12 displays the temperature distribution inside the molten filler metal. For SW-GMAW, the peak temperature of the droplet was higher than 3500 K, as shown in Fig. 12a. Meanwhile, the temperature of the detached droplet was higher than that of undetached droplet; the average temperature of the detached droplet was 3480 K (t=0.038 s). The maximum temperature of the droplet exceeded the boiling point of the wire metal in this simulation probably because the metal evaporation was ignored. Consequently, the influence of metal evaporation on the heat loss has to be calculated in future work to further increase the calculation accuracy. For DW-GMAW,
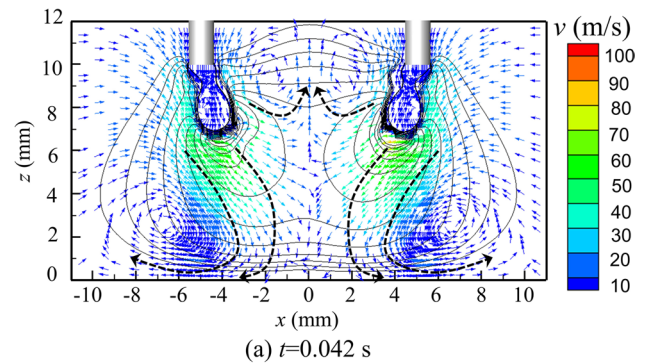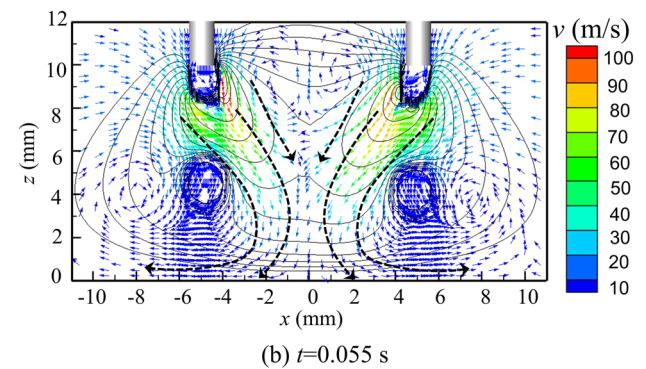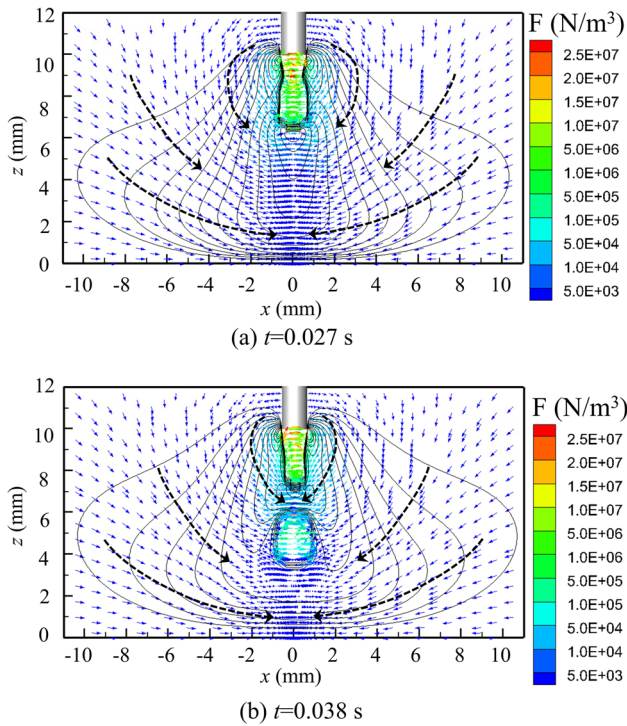
Fig. 8 Electromagnetic force distribution in SW-GMAW

(a) t=0.027 s

(b) t=0.038 s
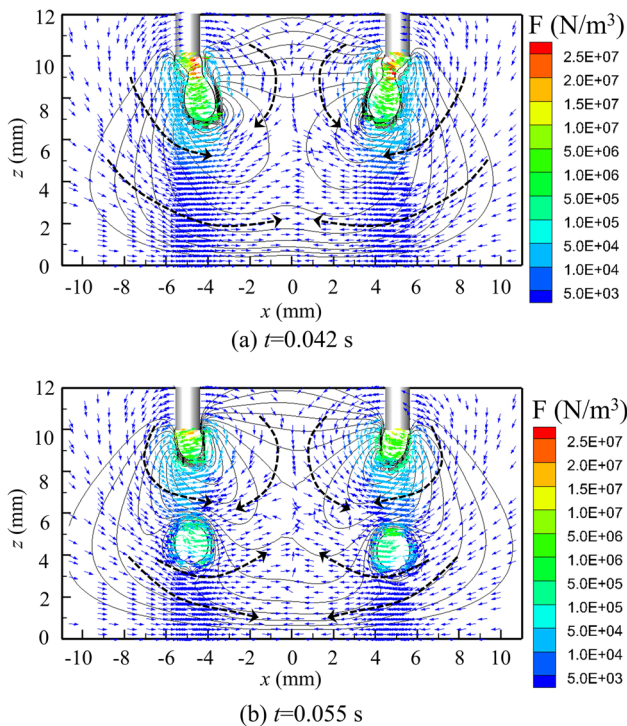
Fig. 9 Electromagnetic force distribution in DW-GMAW
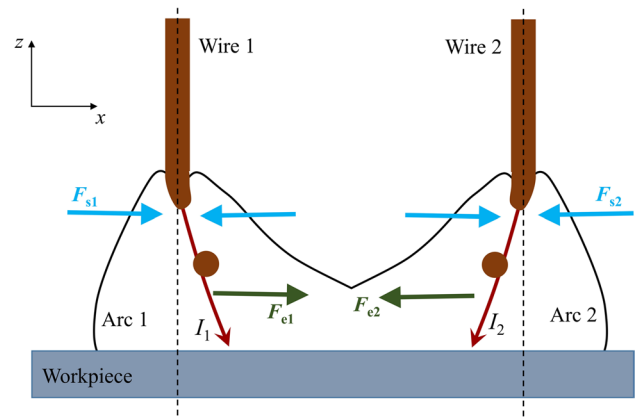
(a) t=0.042 s

(b) t=0.055 s

Fig. 10 Schematic diagram of electromagnetic force acted on the arc in DW-GMAW
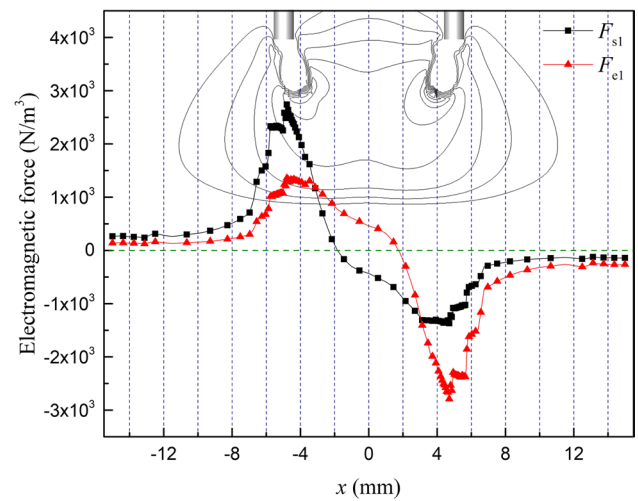

Fig. 11 Comparison of F_{s1} and F_{e1} in DW-GMAW

the high-temperature zone was decreased dramatically. Only at the interface of molten metal and arc plasma, the temperature was higher than 3400 K, as indicated in Fig. 12b. The average temperature of the undetached droplet was about 2940 K ($t = 0.042$ s). The average temperature of the detached droplet was 3020 K ($t = 0.055$ s). It suggests that the arc interaction decreased the temperature of the droplet. Generally, the temperature of the filler metal depends on the following major heat fluxes including the joule heating of the filler metal, the heat conduction from the arc plasma, and the sheath heating at the metal/arc interface. In this study, the same welding current was used in SW-GMAW and DW-GMAW; the distributions of current density in the filler metal were almost the same, so the difference of the joule heating and sheathing heating was less. However, as displayed in Figs. 3 and 4, the maximum temperature around the filler metal showed bigger difference between

Fig. 12 Simulated temperature distribution inside droplet

(a) SW-GMAW   (b) DW-GMAW
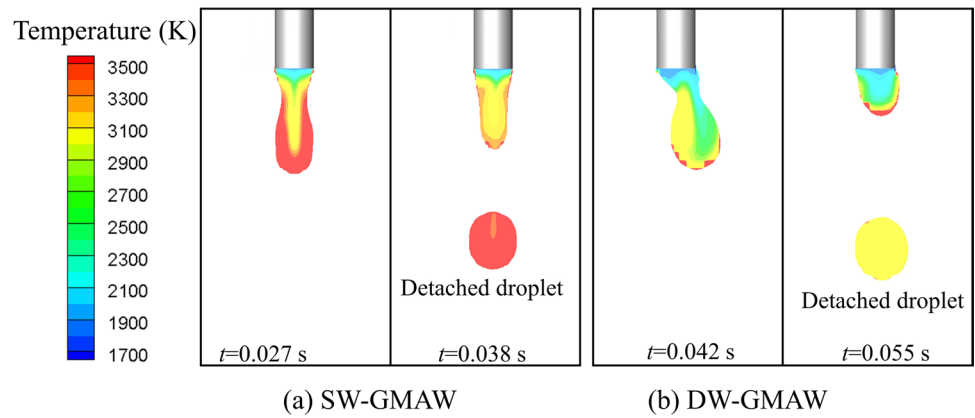
SW-GMAW and DW-GMAW. The higher arc temperature around the filler metal caused higher droplet temperature by the heat conduction. The decrease of the droplet temperature can avoid the overheating of the weld pool to a certain extent, which is helpful to suppress some welding defects like undercutting and humping bead. However, the present model cannot predict the weld pool behavior, so a more unified model containing the interaction of arc-droplet-weld pool needs to be established in the future work.

4 Experimental validation

In order to validate the proposed unified arc-droplet model for DW-GMAW, the results between the experiment of Ding et al. [28] and the simulation were compared. Figure 13 displays the metal transfer cycle obtained by experimental measurement and numerical calculation. The results agreed well. Figure 14 shows the captured images of droplet and calculated droplet shape. The simulated size of the droplet had good agreements with the experiment observation. The simulated inclination angle of the droplet was slightly smaller than that in
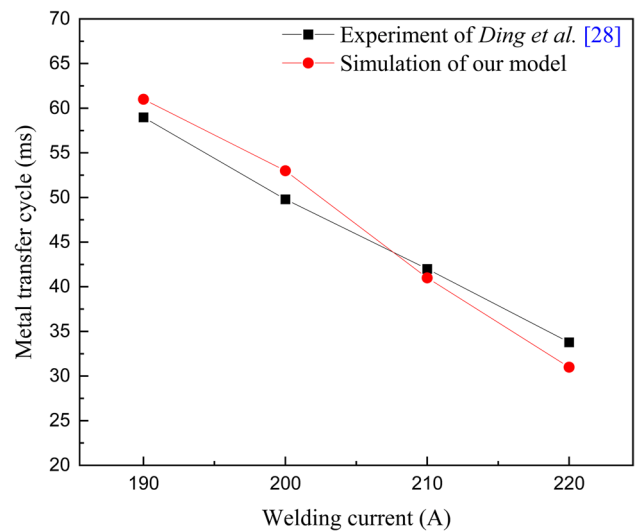
Fig. 13 Comparison of metal transfer cycle between experiment and simulation

experiment. It may be due to the ignorance of the wire inclination, which should be considered reasonably in our future model optimization.

Fig. 14 Comparison of droplet shape between experiment and simulation

(a) Captured images of droplet

(b) Simulated droplet
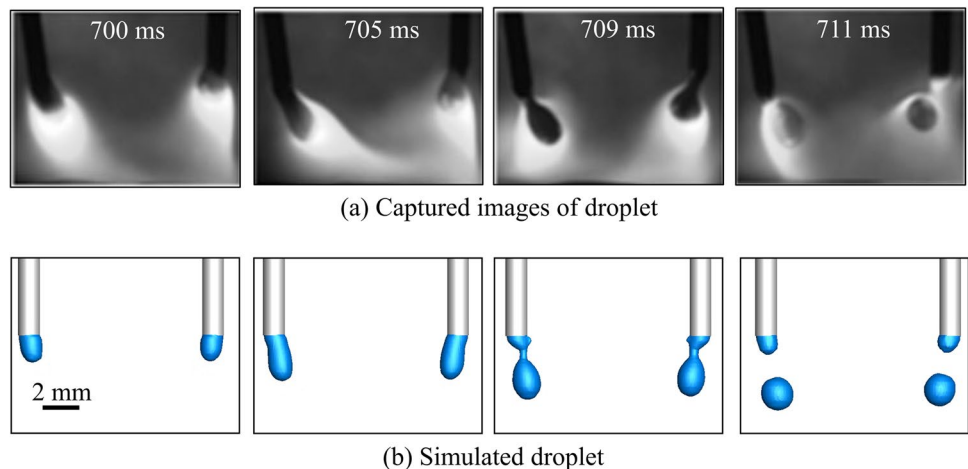
5 Conclusions

(1) The three-dimensional unified arc-droplet models for traditional SW-GMAW and DW-GMAW were established, respectively. The mutual attraction of arc plasma and the inclination of the droplet were numerically calculated.

(2) Compared to DW-GMAW with the unimodal temperate distribution along x-axis, the temperature distribution became bimodal and the peak temperature reduced for DW-GMAW. The peak temperature points were deviated from the wire centers due to the attraction of two arcs. The average temperature of the filler metal also reduced.

(3) The electromagnetic forces acted on each arc can be divided into the self-induced electromagnetic force and additional electromagnetic force. The self-induced electromagnetic force can constrict the arc, while the additional electromagnetic force caused the arc tilt and attraction. The two forces have the same order of magnitude.

Declarations

Conflict of interest The authors declare no competing interests.

References

1. Martina F, Ding J, Williams S et al (2019) Tandem metal inert gas process for high productivity wire arc additive manufacturing in stainless steel. Addit Manuf 25:545–550. https://doi.org/10.1016/j.addma.2018.11.022
2. Chaturvedi M, Scutelnicu E, Rusu CC et al (2021) Wire arc additive manufacturing: review on recent findings and challenges in industrial applications and materials characterization. Metals (Basel) 11:939
3. Jin W, Zhang C, Jin S et al (2020) Wire arc additive manufacturing of stainless steels: A review. Appl Sci 10:1563
4. Devasia BTAJ, Krishna T, Kuruvila MT (2020) Manufacturing of a bimetallic structure of stainless steel and mild steel through wire arc additive manufacturing — a critical review. Int J Innov Sci Res Technol 5:679–685. https://doi.org/10.38124/ijisrt20jun583
5. Kanemaru S, Sasaki T, Sato T et al (2014) Study for TIG-MIG hybrid welding process. Weld World 58:11–18. https://doi.org/10.1007/s40194-013-0090-y
6. Kanemaru S, Sasaki T, Sato T et al (2015) Study for the mechanism of TIG-MIG hybrid welding process. Weld World 59:261–268. https://doi.org/10.1007/s40194-014-0205-0
7. Cho JH, Na SJ (2009) Three-dimensional analysis of molten pool in GMA-laser hybrid welding. Weld J 88:35s–43s
8. Shi C, Zou Y, Zou Z, Wu D (2014) Twin-wire indirect arc welding by modeling and experiment. J Mater Process Technol 214:2292–2299. https://doi.org/10.1016/j.jmatprotec.2014.04.027
9. Gu Y, Hua X, Ye D et al (2017) Numerical simulation of hump suppression in high-speed triple-wire GMAW. Int J Adv Manuf Technol 89:727–734. https://doi.org/10.1007/s00170-016-9119-x
10. Lu Y, Chen S, Shi Y et al (2014) Double-electrode arc welding process: Principle, variants, control and developments. J Manuf Process 16:93–108. https://doi.org/10.1016/j.jmapro.2013.08.003
11. Assunção PDC, Ribeiro RA, Moreira PMGP et al (2020) A preliminary study on the double cold wire gas metal arc welding process. Int J Adv Manuf Technol 106:5393–5405. https://doi.org/10.1007/s00170-020-05005-6
12. Wang L, Wu CS, Gao JQ (2016) Suppression of humping bead in high speed GMAW with external magnetic field. Sci Technol Weld Join 21:131–139. https://doi.org/10.1179/1362171815Y.0000000074
13. Chen J, Zhang Y, Wu C, Padhy GK (2019) Suppression of undercut defects in high-speed GMAW through a compound magnetic field. J Mater Process Technol 274:116288. https://doi.org/10.1016/J.JMATPROTEC.2019.116288
14. Michie K, Blackman S, Ogunbiyi TEB (1999) Twin-wire GMAW: process characteristics and applications. Weld J 78:31–34
15. Sathishkumar M, Bhakat YJ, Kumar KG et al (2021) Investigation of double-pulsed gas metal arc welding technique to preclude carbide precipitates in aerospace grade hastelloy X. J Mater Eng Perform 30:661–684. https://doi.org/10.1007/s11665-020-05360-1
16. Rosli NA, Alkahari MR, bin Abdollah MF et al (2021) Review on effect of heat input for wire arc additive manufacturing process. J Mater Res Technol 11:2127–2145
17. Ren L, Gu H, Wang W, et al (2021) Microstructure and properties of Al-6.0Mg-0.3Sc alloy deposited by double-wire arc additive manufacturing. 3D Print Addit Manuf 9:301–310. https://doi.org/10.1089/3dp.2020.0039
18. Chen D, Chen M, Wu C (2015) Effects of phase difference on the behavior of arc and weld pool in tandem P-GMAW. J Mater Process Technol 225:45–55. https://doi.org/10.1016/j.jmatprotec.2015.05.022
19. Liu G, Tang X, Han S, Cui H (2021) Influence of interwire distance and arc length on welding process and defect formation mechanism in double-wire pulsed narrow-gap gas metal arc welding. J Mater Eng Perform 30:7622–7635. https://doi.org/10.1007/s11665-021-05888-w
20. Wu K, Cao X, Yin T et al (2019) Metal transfer process and properties of double-wire double pulsed gas metal arc welding. J Manuf Process 44:367–375. https://doi.org/10.1016/j.jmapro.2019.06.019
21. Ueyama T, Ohnawa T, Tanaka M, Nakata K (2007) Occurrence of arc interaction in tandem pulsed gas metal arc welding. Sci Technol Weld Join 12:523–529. https://doi.org/10.1179/174329307X173715
22. Moinuddin SQ, Sharma A (2015) Arc stability and its impact on weld properties and microstructure in anti-phase synchronised synergic-pulsed twin-wire gas metal arc welding. Mater Des 67:293–302. https://doi.org/10.1016/j.matdes.2014.11.052
23. Groetelaars PJ, de Morais CO, Scotti A (2009) Influence of the arc length on metal transfer in the single potential double-wire MIG/MAG process. Weld Int 23:112–119. https://doi.org/10.1080/09507110802349643
24. Cai X, Fan C, Lin S et al (2017) Effects of shielding gas composition on arc behaviors and weld formation in narrow gap tandem GMAW. Int J Adv Manuf Technol 91:3449–3456. https://doi.org/10.1007/s00170-017-9990-0
25. Wu K, Xie P, Liu Z et al (2020) Investigation of double arc interaction mechanism and quantitative analysis of double arc offset in high-power double-wire DP-GMAW. J Manuf Process 49:423–437. https://doi.org/10.1016/j.jmapro.2019.10.022

26. Pu J, Wu S, Hu Q, Wang Y (2019) Effect of welding current on arc behavior in tandem GMAW. Int J Mod Phys B 33:1–6. https://doi.org/10.1142/S0217979219400368

27. Schnick M, Wilhelm G, Lohse M et al (2011) Three-dimensional modelling of arc behaviour and gas shield quality in tandem gas-metal arc welding using anti-phase pulse synchronization. J Phys D Appl Phys 44:185205. https://doi.org/10.1088/0022-3727/44/18/185205

28. Ding X, Li H, Yang L, Gao Y (2013) Numerical simulation of metal transfer process in tandem GMAW. Int J Adv Manuf Technol 69:107–112. https://doi.org/10.1007/s00170-013-4999-5

29. Ding X, Li H, Wei H, Liu J (2016) Numerical analysis of arc plasma behavior in double-wire GMAW. Vacuum 124:46–54. https://doi.org/10.1016/j.vacuum.2015.11.006

30. Murphy AB (2011) A self-consistent three-dimensional model of the arc, electrode and weld pool in gas-metal arc welding. J Phys D Appl Phys 44:194009. https://doi.org/10.1088/0022-3727/44/19/194009

31. Lowke JJ, Tanaka M (2006) "LTE-diffusion approximation" for arc calculations. J Phys D Appl Phys 39:3634–3643. https://doi.org/10.1088/0022-3727/39/16/017

32. Xu G, Hu J, Tsai HL (2008) Three-dimensional modeling of the plasma arc in arc welding. J Appl Phys 104:103301. https://doi.org/10.1063/1.2998907

33. Xu G, Hu J, Tsai HL (2009) Three-dimensional modeling of arc plasma and metal transfer in gas metal arc welding. Int J Heat Mass Transf 52:1709–1724. https://doi.org/10.1016/j.ijheatmasstransfer.2008.09.018

34. Zhao Y, Chung H (2017) Numerical simulation of droplet transfer behavior in variable polarity gas metal arc welding. Int J Heat Mass Transf 111:1129–1141. https://doi.org/10.1016/j.ijheatmasstransfer.2017.04.090

35. Zhao Y, Chung H (2018) Influence of power source dynamics on metal and heat transfer behaviors in pulsed gas metal arc welding. Int J Heat Mass Transf 121:887–899. https://doi.org/10.1016/j.ijheatmasstransfer.2018.01.058

36. Murphy AB (2010) The effects of metal vapour in arc welding. J Phys D Appl Phys 43:434001. https://doi.org/10.1088/0022-3727/43/43/434001

37. Zielińska S, Musioł K, Dzierga K et al (2007) Investigations of GMAW plasma by optical emission spectroscopy. Plasma Sources Sci Technol 16:832–838. https://doi.org/10.1088/0963-0252/16/4/019

38. Ogino Y, Hirata Y, Asai S (2017) Numerical simulation of metal transfer in pulsed-MIG welding. Weld World 61:1289–1296. https://doi.org/10.1007/s40194-017-0492-3

39. Ogino Y, Hirata Y, Asai S (2020) Discussion of the effect of shielding gas and conductivity of vapor core on metal transfer phenomena in gas metal arc welding by numerical simulation.

40. Brackbill JU, Kothe DB, Zemach C (1992) A continuum method for modeling surface tension. J Comput Phys 100:335–354. https://doi.org/10.1016/0021-9991(92)90240-Y

41. Tanaka M, Lowke JJ (2007) Predictions of weld pool profiles using plasma physics. J Phys D Appl Phys 40:R1–R23. https://doi.org/10.1088/0022-3727/40/1/R01

42. Lowke JJ (1974) Predictions of arc temperature profiles using approximate emission coefficients for radiation losses. J Quant Spectrosc Radiat Transf 14:111–122. https://doi.org/10.1016/0022-4073(74)90004-1

43. Tashiro S, Tanaka M, Ushio M et al (2006) Prediction of energy source properties of free-burning arcs. Vacuum 80:1190–1194. https://doi.org/10.1016/j.vacuum.2006.01.058

44. Lu F, Wang HP, Murphy AB, Carlson BE (2014) Analysis of energy flow in gas metal arc welding processes through self-consistent three-dimensional process simulation. Int J Heat Mass Transf 68:215–223. https://doi.org/10.1016/j.ijheatmasstransfer.2013.09.021

45. Hu J, Tsai HL (2006) Effects of current on droplet generation and arc plasma in gas metal arc welding. J Appl Phys 100:053304. https://doi.org/10.1063/1.2337261

46. Drazin P (1987) Fluid mechanics. Physics education. CBS College, New York, pp 350–354

47. Wang L, Chen J, Wu CS, Luan SC (2020) Numerical analysis of arc and droplet behaviors in gas metal arc welding with external compound magnetic field. J Mater Process Technol 282:116638. https://doi.org/10.1016/j.jmatprotec.2020.116638

48. Hirata Y (1995) Physics of welding (III) —- melting rate and temperature distribution of electrode wire. Weld Int 9:348–351. https://doi.org/10.1080/09507119509548811

49. MI Boulos, P Fauchais EP (2013) Thermal plasmas: fundamentals and applications. Springer Science & Business Media, New York

50. Murphy AB, Arundelli CJ (1994) Transport coefficients of argon, nitrogen, oxygen, argon-nitrogen, and argon-oxygen plasmas. Plasma Chem Plasma Process 14:451–490. https://doi.org/10.1007/BF01570207